Journal of Lasers in Medical Sciences

J Lasers Med Sci 2026;17:e51117

Original Article

http://journals.sbmu.ac.ir/jlms

doi:10.34172/jlms.51117

Low-Cost Photoacoustic Imaging System for Vascular Occlusion Detection in Polymer Phantoms

Nesbher Vulgira[1], Atika Windra Sari[2], Mika Sillanpää[3,4,5], Mitrayana[1*]

[1]Department of Physics, Faculty of Mathematics and Natural Sciences, Universitas Gadjah Mada, Sekip Utara, Yogyakarta, Indonesia
[2]Department of Physics, Faculty of Sciences and Technology, Institute Technology and Sciences Nahdlatul Ulama Pekalongan, Jl. Karangdowo 9 Kedungwuni, Pekalongan, Indonesia
[3]Saveetha School of Engineering, Saveetha Institute of Medical and Technical Sciences, Saveetha University, Chennai, Tamil Nadu – 602105, India
[4]Institute for Nanotechnology and Water Sustainability (iNanoWS), Florida Campus, College of Science, Engineering and Technology, University of South Africa, Johannesburg, 1710, South Africa
[5]Centre of Research Impact and Outcome, Chitkara University Institute of Engineering and Technology, Chitkara University, Rajpura – 140401, Punjab, India

***Correspondence to**
Mitrayana,
Email: mitrayana@ugm.ac.id

Received: December 9, 2025
Accepted: July 11, 2026
ePublished: September 1, 2026

Abstract

Introduction: Vascular occlusion is a chronic condition that impairs blood flow to vital organs. This study developed a novel, low-cost photoacoustic imaging (PAI) system that utilizes phantom modeling to detect this condition. In this study, vascular occlusion was modeled using polyvinyl chloride–dioctyl terephthalate phantoms, which were categorized into healthy and occluded types.

Methods: The PAI system comprised an 808-nm laser diode as the radiation source, a condenser microphone as the detector, and a mechanical stage for sample scanning. The PAI system utilized a modulated continuous-wave diode laser, operating at a frequency of 14 kHz and a 50% duty cycle.

Results: Acoustic intensity analysis revealed that healthy vasculature consistently generated more intense signals than occluded vasculature. At a depth of 1 mm, the average intensities were 76.3 dB (healthy) and 65.2 dB (occluded), which decreased to 46.2 dB and 22.1 dB, respectively, at a 5-mm depth. Because of these differences, the contrast ratio between healthy and occluded regions ranged from 1.4 to 6.6 dB. Furthermore, the signal-to-noise ratio in healthy samples was measured at 16.1 dB (1 mm depth) and 3.2 dB (5 mm depth).

Conclusion: This study demonstrates that a simple PAI system can distinguish between healthy and occluded vasculature.

Keywords: PAI, Diode laser, Acoustic intensity, Occluded vascular

Introduction

Vascular occlusion occurs when a vascular system becomes restricted or obstructed.[1] According to the World Health Organization, vascular occlusion of the heart is one of the second major causes of death, accounting for 633,842 annual fatalities in the United States, while 17.7 million deaths refer to the global burden of cardiovascular disease reported by the World Health Organization (WHO).[2] Vascular occlusion is the first stage of cardiovascular illness.[3] While clinical examinations can reliably diagnose this condition,[3,4] the potential of photoacoustic imaging (PAI) for assessing vascular occlusion remains largely unexplored.

Vascular occlusion, a rather common condition in the general population, is primarily caused by modifiable risk factors such as a poor diet, physical inactivity, tobacco use, and excessive alcohol consumption.[5] These factors contribute to the formation of atherosclerotic plaque—composed of fat, cholesterol, and other substances—along the arterial walls.[6] This buildup narrows the vessels, reducing the blood flow to vital organs and other parts of the body.[7] If untreated, the impaired circulation can cause major complications, including heart attacks, strokes, and other cardiovascular diseases.[1,3,4,6]

Vascular occlusion is currently detected using techniques such as X-ray angiography, computed tomography angiography, magnetic resonance angiography, and Doppler ultrasonography.[8–11] Despite their widespread use, they have limitations such as inadequate soft tissue contrast for vascular imaging,[8,9] exposure to ionizing radiation, the need for iodine-based contrast agents, high cost, motion sensitivity, poor spatial resolution, and the fundamental limitation of measuring blood flow without yielding optical or molecular data.[12]

Please cite this article as follows: Vulgira N, Sari AW, Sillanpää M, Mitrayana. Low-cost photoacoustic imaging system for vascular occlusion detection in polymer phantoms. J Lasers Med Sci 2026;17: e51117. doi: https://doi.org/10.34172/jlms.51117

PAI is a hybrid modality that generates high-resolution images based on the optical laser-light absorption by biological tissues to generate acoustic waves.[13] In this technique, the absorption of modulated continuous-wave (CW) laser light by tissues causes harmonic thermal expansion, generating acoustic signals that are detected to form detailed vascular images.[14,15]

The photoacoustic (PA) effect, also referred to as the optoacoustic effect, occurs when a material absorbs modulated electromagnetic light and consequently generates sound waves.[16,17]. This phenomenon was first documented by Alexander Graham Bell in the late 19th century. Bell discovered that light absorption induced sound in solids via thermal expansion caused by localized heating.[18] Although its practical utility remained unrealized for decades, the later development of sophisticated laser and ultrasound detectors laid the foundation for PAI. Since the early 2000s, PAI has matured into a popular biomedical imaging technique owing to its unique capacity to merge the high resolution of ultrasound with the superior optical contrast of biological tissues.[19]

PAI is based on the principle of converting light energy into acoustic signals through optical absorption and thermoelastic expansion.[18] First, a modulated continuous-wave (CW) laser, typically in the infrared range, illuminates biological tissues. Chromophores (or natural photoabsorbers) within the tissues absorb this light energy, inducing a rapid, localized temperature rise.[20] This heating triggers thermoelastic expansion, generating broadband ultrasonic waves (pressure waves).[18] These waves propagate through the tissue and are detected by an acoustic sensor, such as an ultrasonic transducer.[21] In this study, a point-by-point X-Y raster scanning approach is implemented to acquire photoacoustic data. Instead of using complex and time-consuming tomographic reconstruction algorithms, straightforward Maximum Amplitude Projection (MAP) mapping is utilized to generate high-contrast 2D vascular occlusion profiles in real-time.

PAI is highly advantageous for medical imaging owing to its sensitivity to key chromophores in biological tissues, such as hemoglobin, water, lipids, and melanin, which have high optical absorption coefficients.[22] When light interacts with tissues, it undergoes absorption, scattering, and reflection.[23] Among these mechanisms, absorption is the most critical one for PAI—the absorbed light energy is converted into heat, which subsequently generates acoustic waves through thermoelastic expansion.[24] This principle enables PAI to noninvasively detect physiological changes—such as blood oxygenation, vascular density, and lesions or obstructions—with high sensitivity and in real time.[25]

The primary advantage of PAI is its noninvasive nature and high spatial resolution, which enable the detailed visualization of vasculature without using ionizing radiation.[26] Furthermore, PAI provides rich optical absorption information for assessing the tissue state, is cost-effective and efficient, and has no aftereffects.[4,27–29] Consequently, PAI holds much promise for detecting cardiovascular disease both before and after the onset of clinical symptoms.[13]

Phantoms serve as a crucial tool for testing and validating PAI systems before their clinical deployment.[30] These models are often made of polymers with tissue-mimicking acoustic and optical properties. They allow researchers to simulate pathological conditions such as atherosclerosis and verify whether a technique or device performs as intended, yielding reliable data.[31,32] Numerous studies have established a strong correlation between consistent phantom testing results and a system's accuracy in in vivo experiments, highlighting the pivotal role of the phantom in transitioning a technology from the lab stage to the clinical stage.[31,33]

Current medical vascular occlusion detection methods have several limitations, including the need for ionizing radiation (which may damage healthy cells), the need for contrast agents (which can induce allergic reactions in patients), high cost, and sensitivity to movement.[8–11] Against this backdrop, PAI can help to overcome the limitations of current vascular occlusion detection methods. PAI has several advantages, including the use of biologically safe, nonionizing radiation, the absence of contrast chemicals, low cost, and noninvasive quality.[4,27–29]

Nd: YAG lasers are commonly used in existing PAI systems.[34,35] Nd: YAG laser generators on a research scale are often huge and heavy, and they need a significant amount of laboratory space. This limits the portability of photoacoustic systems for clinical applications at the patient's bedside.[36] Unlike high-cost pulsed laser systems (e.g., Nd: YAG), the modulated CW diode laser significantly reduces the overall instrumentation cost, making it highly accessible for clinical settings. The compact size of diode lasers enables the development of a portable, bedside-friendly photoacoustic imaging device. By avoiding the high peak power of pulsed lasers, the CW system minimizes the risk of thermal damage to biological tissues, adhering strictly to safety thresholds. As a result, the PAI system created employs a diode laser, which is significantly more compact, affordable, and portable. Therefore, this study aims to develop a tissue-mimicking phantom model and investigate the feasibility of continuous-wave diode laser photoacoustic imaging to enhance vascular occlusion detection.

Materials and Methods

Tissue-mimicking phantoms made of polyvinyl chloride–dioctyl terephthalate (PVC-DOTP) were used to model biological tissues, particularly soft tissues such as muscle and blood vessels. The choice of PVC-DOTP was motivated by its favorable characteristics: stable physical properties, an elastic yet dense structure, ease of shaping, and tunable optical properties achieved by incorporating dyes or light-absorbing particles.[37] Owing to these features, the phantom's absorption coefficient can be customized for specific wavelengths.

The phantom fabrication process involved several steps. First, a 1:5 PVC: DOTP mixture was homogenized using a magnetic stirrer at 200°C. Once uniform, the solution

was transferred to a petri dish to cool and solidify at room temperature (25°C). Prior to the complete hardening of the mixture, a plastic tube was inserted to form a channel resembling a blood vessel. To replicate vascular occlusion, molten wax was first injected into the channel to create a blockage; subsequently, artificial blood was perfused to simulate circulation. This approach yielded a realistic biological model for validating the capability of the PAI system to identify vascular occlusions. The artificial blood mimic consisted of a commercial water-soluble food-grade red dye formulation (primarily composed of purified water and red colorant agents). Although its optical absorption coefficient is lower at the 808-nm wavelength compared to the visible spectrum, the concentration utilized provided a stable and detectable photoacoustic response under the system's 14 kHz modulation protocol. The photoacoustic imaging process is shown in Figure 1.

The PAI setup (Figure 2) consisted of a diode laser (M5-808-0500-0XX, Sunshine-Electronics, China) operated at 808 nm with a maximum power of 500 mW and a condenser microphone (ECM8000, Behringer, Germany) as the acoustic detector. Both components were mounted on a computer numerical control (CNC) platform driven by a NEMA 17 stepper motor (Zhongshan Shengyang Motor Co., Ltd., China), which facilitated raster scanning along the x and y axes. An Arduino Uno microcontroller (ATmega328P, Arduino.cc, Italy) modulated the laser, while the CNC (Chinese CNC Machine, China) controlled the stage movement. The laser beam was focused onto the sample via a convex lens. The sample was placed under the laser and detector, and it generated a PA signal upon absorption of the laser light. This signal was captured by the microphone, processed, and subsequently displayed on a personal computer using LabVIEW software (National Instruments, USA).

System components such as the laser, microphone, and stepper motor were calibrated. Laser calibration was performed in two stages: First, the proportional relationship between the duty cycle and laser power intensity was established. The modulation frequency was maintained constant while the duty cycle was varied from 10% to 90%, and an optical power meter measured the corresponding output power at each interval. These data were used to plot a linear graph of duty cycle versus laser power. Second, the temporal stability of the laser output was assessed. At a constant modulation frequency, the laser power was monitored at 5-minute intervals over 150 minutes for 30%, 40%, and 50% duty cycles. The results of this stability test were plotted as laser power over time.

The microphone was calibrated by comparing its

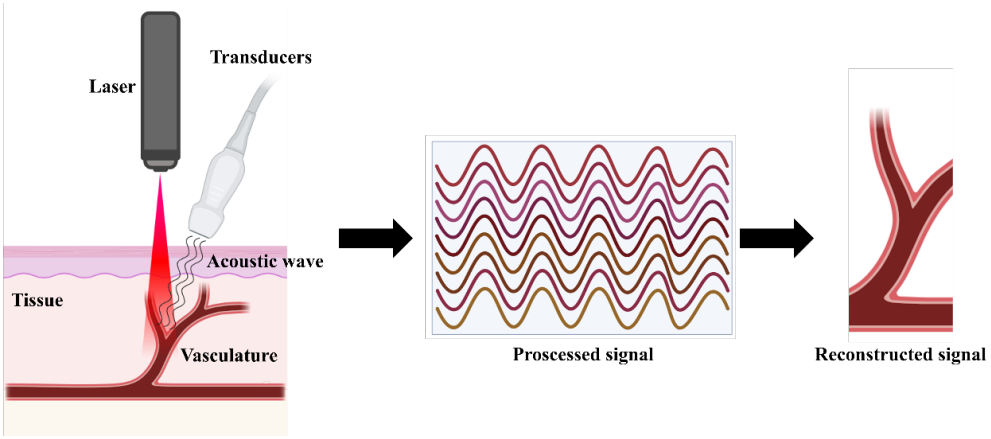

Figure 1. Workflow of photoacoustic imaging (PAI)

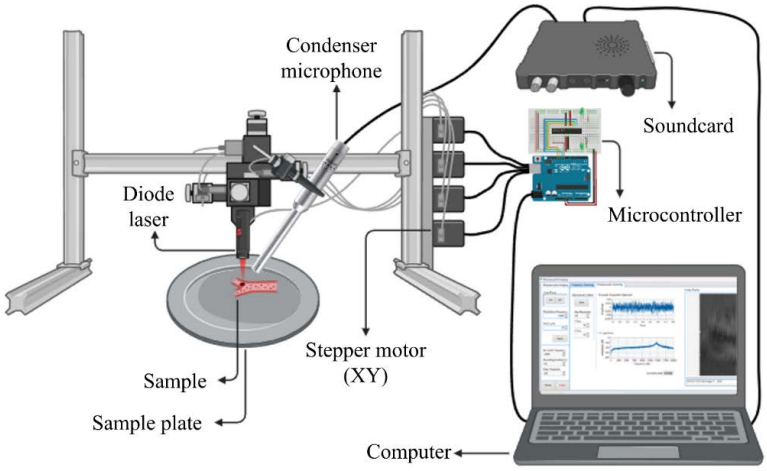

Figure 2. PAI system setup

output against a set of reference frequencies. The detected frequencies of the microphone were recorded and plotted against the reference values on a linear graph to evaluate the consistency of its frequency response. To mitigate the acoustic impedance mismatch and minimize insertion loss at the phantom-air interface, the condenser microphone was positioned as close as possible to the phantom surface without physical contact. This optimal proximity minimized acoustic attenuation through the air gap, while the 14 kHz modulation ensured a high signal-to-noise ratio.

The displacement accuracy of the stepper motor was characterized by comparing its measured travel distance against the commanded values. After determining the step size of the motor, the displacement was tested by commanding a range of 10–50 steps. The actual distance moved by the system was physically measured for each command set. This calibration procedure was performed separately for the *x* and *y* axes. Finally, a linear graph of the average measured displacement was plotted against the ideal displacement to quantify the accuracy.

The data processing protocol did not involve formal tomographic reconstruction. To generate the 2D images, the maximum peak-to-peak amplitude of the 14 kHz modulated photoacoustic signal was extracted at each (X, Y) coordinate. These raw amplitude values were then linearly mapped into a matrix to construct a 2D Maximum Amplitude Projection (MAP) plot representing the structural layout of the vascular phantom.

Five phantom models were developed to represent healthy and obstructed vessels. Each phantom contained vessels at five depths: 1, 2, 3, 4, and 5 mm. These depth variations were introduced to simulate diverse imaging conditions and to evaluate system performance at different penetration levels. The acquired images were subsequently analyzed by examining the cross-sectional amplitude profiles and the average acoustic intensity of the healthy and occluded vascular models. To ensure data reliability and reduce noise, image acquisition for each sample was repeated five times, and the average values were utilized for final analysis.

Results

Figure 3a shows the relationship between duty cycle and laser power. The results indicate a direct correlation between laser radiation power and duty cycle: an increase in duty cycle leads to a proportional increase in the amount of light energy delivered to the object. Figure 3b shows the relationship between laser radiation power and time. At a 50% duty cycle, the laser output remains stable within the range of 0.161–0.162 W. The effective maximum working beam density was maintained at 20 mJ/cm^2, which is considerably lower than the safety threshold of 100 mJ/cm^2.[38] The graph further demonstrates that the laser output power remains generally stable throughout the 150-minute operation, confirming that the system delivers consistent performance.

Figure 3c shows the relationship between the reference frequency and the frequency detected by the microphone. The process of frequency detection by the microphone is illustrated using LabVIEW. The results confirm that the employed microphone accurately detects and distinguishes sound frequency magnitudes.

Figures 3d and 3e present the shift stability of the sample table along the *x* and *y* axes, respectively. Calibration in both directions is considered satisfactory when the mapping data reveal a strong linear correlation between the average measured displacement and the ideal displacement on both axes. Satisfactory calibration implies that the motor movement is both precise and accurate, as expected from the CNC control program. Stepper motor calibration was performed, achieving a single shift step of 0.2 mm. These results confirm that no part of the sample was scanned more than once, if at all.

The laser duty cycle was characterized at a modulation frequency of 14 kHz with values of 10%, 20%, 30%, 40%, 50%, 60%, 70%, 80%, and 90%. The highest acoustic intensity was observed at a 50% duty cycle, with a value of −0.00005 dB (Figure 3f). This optimal duty cycle was selected to ensure the efficient absorption of laser energy in the sample. The raw acoustic voltage signal was converted to a relative logarithmic decibel (dB) scale using the equation $dB = 20\log_{10}\left(\frac{V}{V_{ref}}\right)$[39], where V_{ref} represents the baseline peak voltage obtained during system calibration. The relative acoustic intensity values close to zero (-0.000005 to -0.000009 dB) indicate that the detected signals across various duty cycles maintained high proximity to the calibrated baseline level.

Figure 4 shows the results of PAI for both healthy and occluded vascular phantoms. Figure 5 shows the cross-sectional amplitude profile analysis along with the average acoustic intensity. As shown in Figure 5, occluded vasculature consistently exhibited lower PA emission amplitudes than healthy vessels and empty tubes. This trend was evident across all depths, from shallow vessels (1 mm) to deeper vessels (5 mm). The cross-sectional amplitude profiles at different depths revealed oscillations in the PA signal range. These fluctuations were most likely caused by surface irregularities of the phantom, which create an uneven signal distribution, as well as by the reflection or diffraction of acoustic waves within the phantom medium, resulting in interference patterns that are manifested as variations in the recorded signal.

Figure 6 shows the average acoustic intensity across the five phantom depths. The results show a consistent decrease in signal strength for both healthy and obstructed vessels as depth increases. At a depth of 1 mm, the average acoustic intensity was 76.3 dB for healthy vessels and 65.2 dB for obstructed vessels. At a depth of 5 mm, the intensity decreased to 46.2 and 22.1 dB in healthy and occluded vessels, respectively. The contrast ratio between healthy and obstructed vessels was in the range of 1.4–6.6 dB. In addition, the signal-to-noise ratios of healthy samples were 16.1 dB at 1 mm depth and 3.2 dB at 5 mm depth.

Discussion

This study developed a PAI method for visualizing vascular

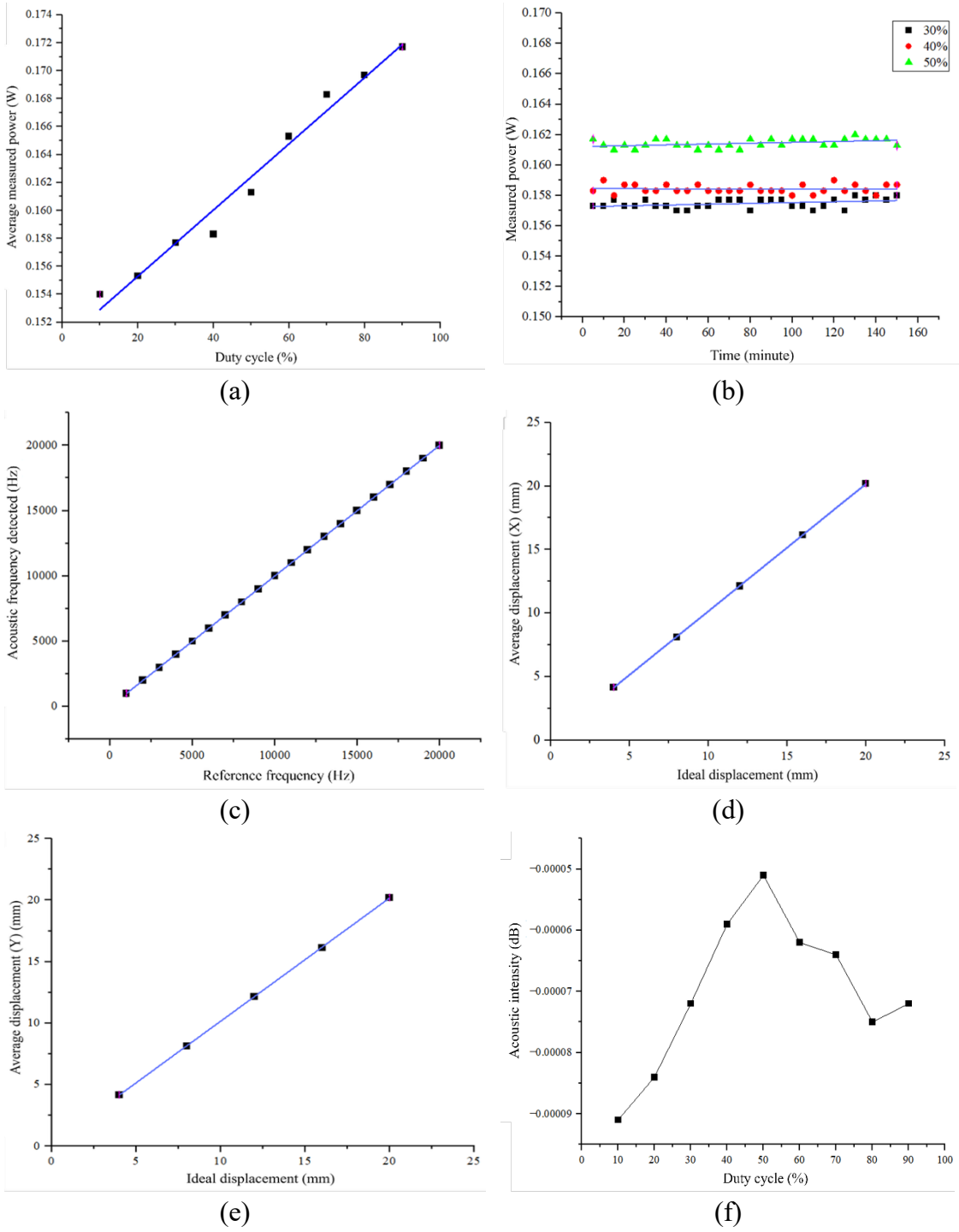

Figure 3. Calibration of the PAI system. (a) Calibration of laser radiation power characteristics as a function of duty cycle. (b) Relationship between laser radiation output and operating time. (c) Correlation between the acoustic signal frequency detected by the microphone and the reference frequency of the generator. (d) Average displacement per step along the *x*-axis. (e) Average displacement per step along the *y*-axis. (f) Acoustic intensity level under a 14 kHz duty cycle

occlusion based on acoustic intensity measurements. The system employed nonionizing radiation and utilized an 808-nm laser, a condenser microphone detector, and an *x*–*y* axis scanning device. Each component was calibrated in advance to ensure proper operation.

In previous studies, the laser and the detector were kept stationary while the test sample was moved along the *x*–*y* axes.[28,40] This approach can lead to undesirable sample shifts. To address this problem, the present system was designed to achieve greater stability by keeping the test sample static while the laser and microphone performed the scanning. The PAI system developed in this study was a PA microscopy (PAM) device with minimal components, capable of imaging polymer phantoms.

PAI is based on the PA effect[41]—the generation of sound waves induced by modulated radiation interacting with biological materials [16]. Hemoglobin, a natural photoabsorber or chromophore present in biological tissues—particularly within blood vessels—plays a key role in PAI.[42] This chromophore interacts with the incoming radiation, and its absorption coefficient at an 808-nm laser wavelength is 8.0 cm^{-1}.[43] Irradiation of biological tissues by

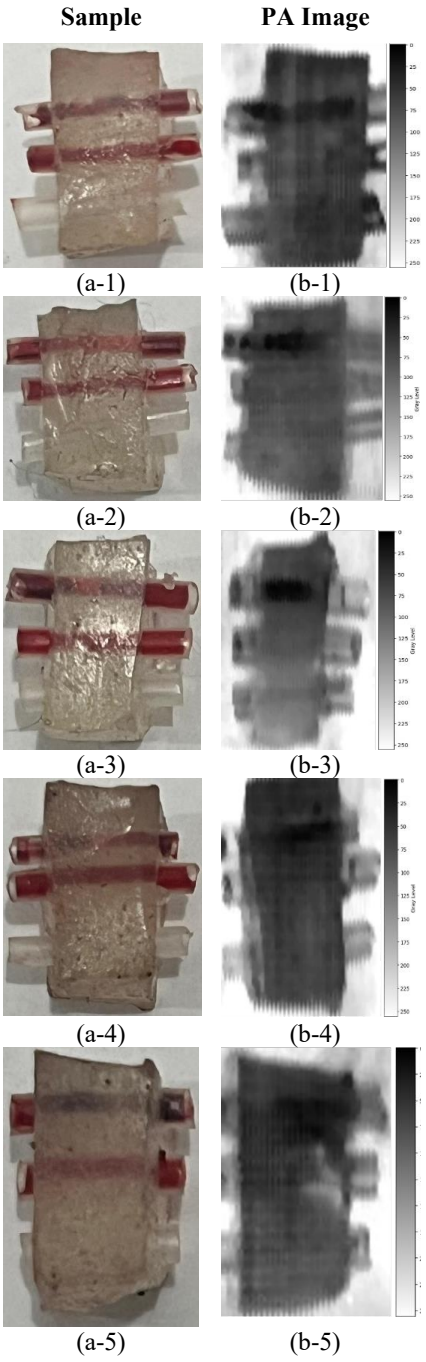

Figure 4. Vascular phantom samples at depths of (a-1) 1 mm, (a-2) 2 mm, (a-3) 3 mm, (a-4) 4 mm, and (a-5) 5 mm. PA images of the vascular phantoms at depths of (b-1) 1 mm, (b-2) 2 mm, (b-3) 3 mm, (b-4) 4 mm, and (b-5) 5 mm

modulated radiation induces localized heating; the heat subsequently diffuses into the surrounding tissue. This thermal effect produces temperature variations that cause pressure changes, which propagate as acoustic waves.[18] These acoustic signals are reconstructed into images,[44] and the resulting sound intensity is used to differentiate healthy from occluded vasculature.

Changes in the pressure of a medium in which acoustic waves are generated can be expressed, as shown in Equation (1).[25]

$$p_0 = \Gamma.\mu_a.F = \frac{\beta c^2}{C_p}\mu_a F \quad (1)$$

where p_0 is the pressure change; μ_a is the absorption coefficient (cm^{-1}); Γ is Grüneisen's coefficient and is expressed as $\Gamma = \frac{\beta c^2}{C_p}$, indicating the thermal and mechanical properties of the tissue; F is the fluence (J/cm^2).[27,43]

A PAI system employing a diode laser was used to detect vascular occlusion. Analysis of the average acoustic intensity across different depths revealed that the deeper the signal source, the lower the measured acoustic intensity. This variation was caused by light attenuation within the phantom material and damping of the acoustic wave before it reached the microphone. At all depths, healthy vasculature consistently produced stronger signals than obstructed vessels, demonstrating the capability of the system to differentiate the optoacoustic properties of the two conditions. Normal flow of blood, a strong chromophore, generates a more intense signal than blood flow hindered by obstructions such as wax.

Vascular occlusion in clinical settings can be detected by various methods (e.g., angiography, electrocardiography, and magnetic resonance angiography) that rely on X-rays, contrast agents, or magnetic fields to visualize vascular conditions.[8–11] These approaches are considered the gold standard for assessing vascular occlusion.[45] However, such techniques often require ionizing radiation, which may damage healthy surrounding tissues. In addition, contrast agents can trigger allergic reactions in certain individuals,[46] while the use of strong magnetic fields may cause discomfort in patients, particularly those with claustrophobia.[47]

The study identified acoustic intensity values that can be used to distinguish healthy and occluded vasculature. The findings suggest that the PAI system has the potential to be developed into a noninvasive, low-cost tool for detecting arterial occlusions in clinical settings. However, the PA system employed in this study was built using relatively simple components. Therefore, further refinement and optimization are required before it can be applied in clinical practice.

Medical researchers previously investigated ultrasound-based PAI (PA-US).[20] This imaging approach typically requires a large and costly laser; in contrast, the present study utilized a compact and inexpensive diode laser. Future research should address the challenges associated with implementing PAI in clinical settings, with a focus on developing patient-friendly systems that utilize portable detectors.

This study demonstrates the capability of a PAI system to distinguish obstructed and healthy arteries. An increase in imaging depth results in a reduced acoustic intensity and image quality, primarily because of light attenuation and acoustic wave damping within the phantom medium. However, this study has limitations as it was conducted on a polymer phantom, and further comparisons with other imaging modalities are necessary to fully evaluate the effectiveness of PAI in detecting arterial occlusion.

Conclusion

This study aimed to demonstrate a noninvasive, low-cost

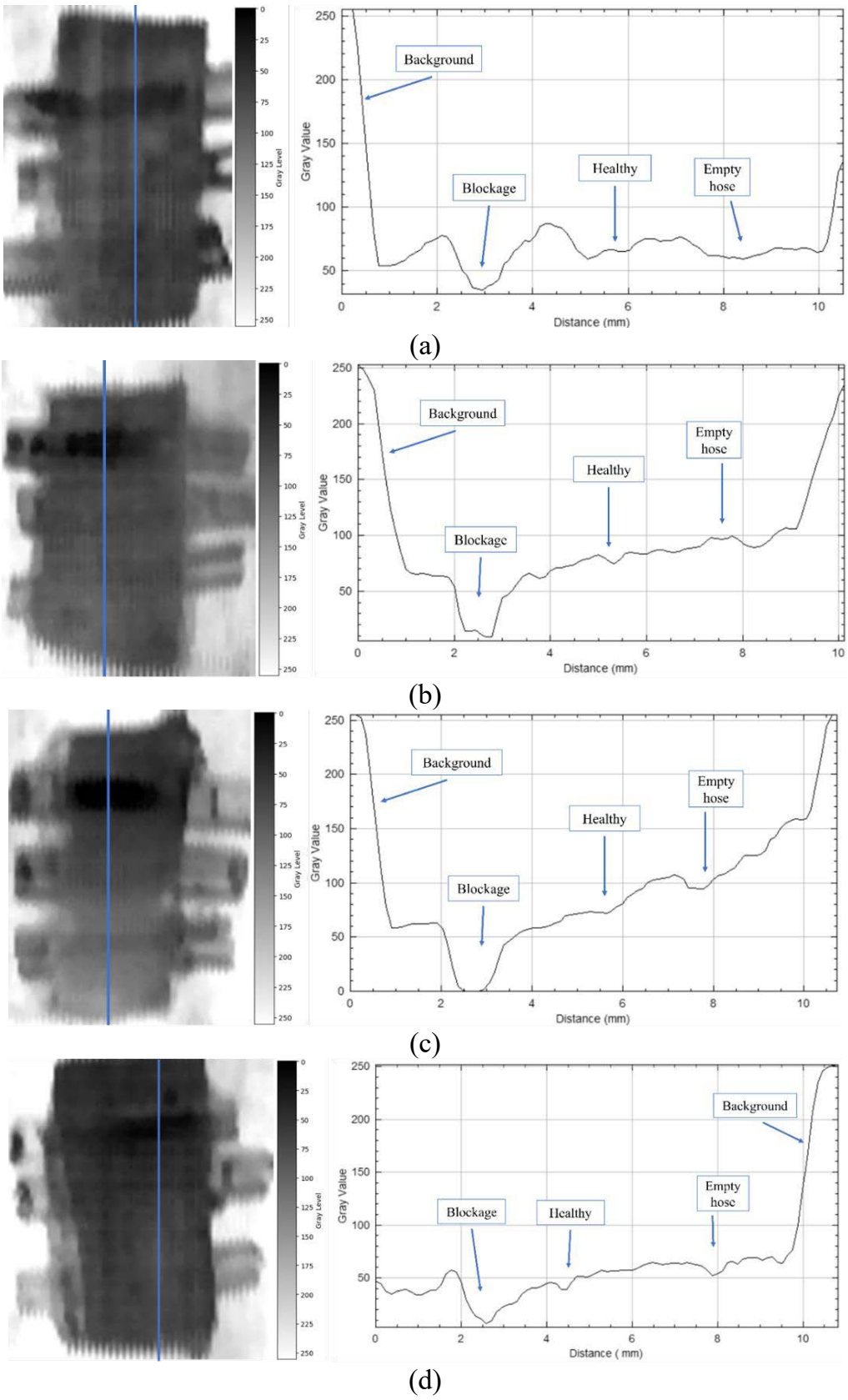

Figure 5. Cross-sectional amplitude profiles of the PA signal at different vascular depths: (a) 1 mm, (b) 2 mm, (c) 3 mm, (d) 4 mm, and (e) 5 mm

imaging system for identifying arterial occlusion. The primary components of the PAI system—including a diode laser, a condenser microphone, and an *x*–*y* axis mechanical scanning system—were calibrated to ensure efficient sample scanning. The laser duty cycle and modulation frequency were set at 50% and 14 kHz, respectively. The results revealed that healthy vasculature consistently exhibited higher acoustic intensity than obstructed vessels—the PA images were clear even at a depth of 5 mm. These findings confirmed the effectiveness of this low-cost system for the

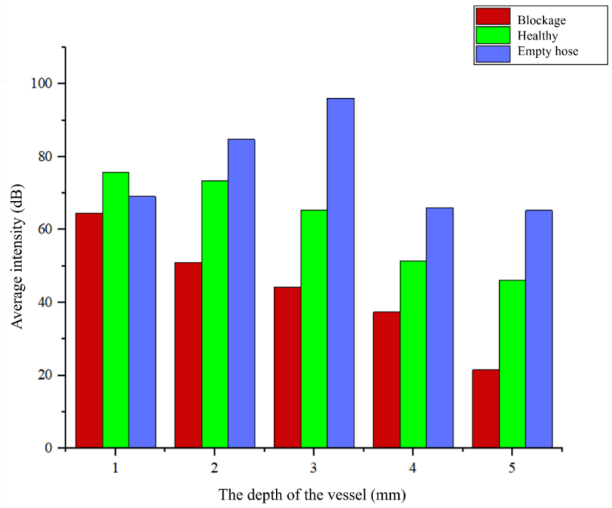

Figure 6. Average acoustic intensity of healthy, occluded, and empty vasculature at different depths

noninvasive detection of arterial occlusions and highlighted its potential as a simple, affordable imaging technique for early vascular disease screening. Moreover, this basic PAI system can be further developed into a tomographic imaging platform that employs only portable components and is capable of real-time scanning.

Acknowledgments

This study was supported by Department of Physics, Faculty of Mathematics and Natural Sciences, Universitas Gadjah Mada.

Authors' Contribution

Conceptualization: Nesbher Vulgira
Data curation: Nesbher Vulgira
Formal analysis: Nesbher Vulgira
Investigation: Nesbher Vulgira
Methodology: Nesbher Vulgira
Project administration: Atika Windra Sari
Resources: Atika Windra Sari
Software: Nesbher Vulgira
Supervision: Mitrayana
Validation: Mitrayana
Visualization: Atika Windra Sari
Writing–original draft: Atika Windra Sari
Writing–review & editing: Mika Sillanpää, Mitrayana

Competing Interests

The authors declare no conflict of interest.

Ethical Approval

This study did not involve human participants or animal subjects. Therefore, ethical approval from an institutional review board or bioethics committee was not required. The experiments were conducted using inanimate polymer phantoms in a controlled laboratory environment. All laboratory safety protocols, particularly regarding laser safety and chemical handling for phantom fabrication, were strictly followed.

Funding

This research was funded by the Ministry of Higher Education, Science, and Technology of the Republic of Indonesia through the Master's Thesis Research Grant (Penelitian Tesis Magister/PTM) under Contract Number: 1103/UN1/DITLIT/Dit-Lit/PT.01.03/2026.

References

1. Murray G, Convery C, Walker L, Davies E. Guideline for the management of hyaluronic acid filler-induced vascular occlusion. J Clin Aesthet Dermatol 2021;14(5): E61-9.
2. Naveed A, Atique R, Saeed HA, Sharif J, Haidar A, Samad A. Cardiovascular diseases: understanding the leading cause of death worldwide. Global Journal of Multidisciplinary Sciences and Arts 2024;1(1):100-10. doi:10.70445/gjmdsa.1.1.2024.100-110
3. Hu K, Li Y, Ke Z, Yang H, Lu C, Li Y, et al. History, progress and future challenges of artificial blood vessels: a narrative review. Biomater Transl 2022;3(1):81-98. doi:10.12336/biomatertransl.2022.01.008
4. Altalhi R, Pechlivani N, Ajjan RA. PAI-1 in diabetes: pathophysiology and role as a therapeutic target. Int J Mol Sci 2021;22(6):3170. doi:10.3390/ijms22063170
5. Jalali Z, Khademalhosseini M, Soltani N, Esmaeili Nadimi A. Smoking, alcohol and opioids effect on coronary microcirculation: an update overview. BMC Cardiovasc Disord 2021;21(1):185. doi:10.1186/s12872-021-01990-y
6. Miceli G, Basso MG, Pintus C, Pennacchio AR, Cocciola E, Cuffaro M, et al. Molecular pathways of vulnerable carotid plaques at risk of ischemic stroke: a narrative review. Int J Mol Sci 2024;25(8):4351. doi:10.3390/ijms25084351
7. Młynarska E, Czarnik W, Fularski P, Hajdys J, Majchrowicz G, Stabrawa M, et al. From atherosclerotic plaque to myocardial infarction-the leading cause of coronary artery occlusion. Int J Mol Sci 2024;25(13):7295. doi:10.3390/ijms25137295
8. Sharina I, Awad R, Cobb S, Martin E, Marrelli SP, Reddy AK. Non-invasive real-time pulsed Doppler assessment of blood flow in mouse ophthalmic artery. Cell Rep Methods 2025;5(2):100983. doi:10.1016/j.crmeth.2025.100983
9. Becker LM, Peper J, van Nes SH, van Es HW, Sjauw KD, van de Hoef TP, et al. Non-invasive physiological assessment of coronary artery obstruction on coronary computed tomography angiography. Neth Heart J 2024;32(11):397-404. doi:10.1007/s12471-024-01902-7
10. Li W, Zhang R, Zhang X, Wu S, Ma T, Hou Y, et al. Precise diagnosis of cardiac-cerebral vascular diseases with magnetic resonance imaging-based nanoprobes. iRadiology 2024;2(3):264-84. doi:10.1002/ird3.87
11. Bankole ND, Dujardin PA, Bala F, Ehrmann S, Desplobain K, Patat F, et al. Transcranial doppler ultrasound for the diagnosis of large vessel occlusion in patients with acute ischemic stroke: a systematic review. Clin Neurol Neurosurg 2024;245:108506. doi:10.1016/j.clineuro.2024.108506
12. Wen Y, Guo D, Zhang J, Liu X, Liu T, Li L, et al. Clinical photoacoustic/ultrasound dual-modal imaging: current status and future trends. Front Physiol 2022;13:1036621. doi:10.3389/fphys.2022.1036621
13. Kye H, Kang MS, Jo D, Park B, Jang HJ, Kim J, et al. Advances in high-resolution photoacoustic imaging techniques for cellular visualization. View (Beijing) 2026;7(1):20250125. doi:10.1002/VIW.20250125
14. Yang H, Li D, Yang J, Wang J, Gan S, Cao K, et al. Study on preparation and properties of PAI materials containing trifluoromethyl in side chain. Macromol Res 2021;29(10):727-34. doi:10.1007/s13233-021-9077-5
15. Çınar S, Gerçek AE, Bilgiç AE, Özdemir Ö. Automated noise removal system for photoacoustic imaging using independent component analysis. Digit Signal Process 2025;159:105004. doi:10.1016/j.dsp.2025.105004
16. Julianto R, Mujtahid Anas A, Mitrayana. Characterization of photoacoustic tomography based on 450 nm visible light and its application for detection of formalin fish meat. J Phys Conf Ser 2023;2498(1):012015. doi:10.1088/1742-6596/2498/1/012015
17. Wu J, Peng Z, Zhang X, He W, Yang C. Wavelet-ResNet: a deep residual network combined with wavelet transform for photoacoustic blood glucose detection. Biomed Signal Process Control 2024;97:106718. doi:10.1016/j.bspc.2024.106718
18. Neelamraju PM, Gundepudi K, Sanki PK, Busi KB, Mistri TK,

Sangaraju S, et al. Potential applications for photoacoustic imaging using functional nanoparticles: a comprehensive overview. Heliyon 2024;10(15): e34654. doi:10.1016/j.heliyon.2024.e34654
19. Neprokin A, Broadway C, Myllylä T, Bykov A, Meglinski I. Photoacoustic imaging in biomedicine and life sciences. Life (Basel) 2022;12(4):588. doi:10.3390/life12040588
20. Chen Z, Gezginer I, Zhou Q, Tang L, Deán-Ben XL, Razansky D. Multimodal optoacoustic imaging: methods and contrast materials. Chem Soc Rev 2024;53(12):6068-99. doi:10.1039/d3cs00565h
21. Manwar R, Zafar M, Xu Q. Signal and image processing in biomedical photoacoustic imaging: a review. Optics 2020;2(1):1-24. doi:10.3390/opt2010001
22. Zhang Y, Li Z, Du Z, Pan J, Huang Y. Multifunctional upconversion nanoparticles transforming photoacoustic imaging: a review. Nanomaterials (Basel) 2025;15(14):1074. doi:10.3390/nano15141074
23. Ahmed KK, Muheddin DQ, Mohammed PA, Ezat GS, Murad AR, Ahmed BY, et al. A brief review on optical properties of polymer composites: insights into light-matter interaction from classical to quantum transport point of view. Results Phys 2024;56:107239. doi:10.1016/j.rinp.2023.107239
24. Lembessis VE, Andrews DL. Forces in the interaction of light with matter. Appl Sci 2024;14(16):7008. doi:10.3390/app14167008
25. Hosseinaee Z, Le M, Bell K, Haji Reza P. Towards non-contact photoacoustic imaging [review]. Photoacoustics 2020;20:100207. doi:10.1016/j.pacs.2020.100207
26. Pang W, Yuan C, Zhong T, Huang X, Pan Y, Qu J, et al. Diagnostic and therapeutic optical imaging in cardiovascular diseases. iScience 2024;27(11):111216. doi:10.1016/j.isci.2024.111216
27. Windra Sari A, Widyaningrum R, Setiawan A, Mitrayana. Photoacoustic imaging of gingival inflammation using low-cost near-infrared diode laser. Appl Acoust 2024;218:109903. doi:10.1016/j.apacoust.2024.109903
28. Windra Sari A, Widyaningrum R, Yana M. Photoacoustic imaging for periodontal disease examination. J Lasers Med Sci 2022;13: e37. doi:10.34172/jlms.2022.37
29. Windra Sari A, Widyaningrum R, Setiawan A, Mitrayana. Recent development of photoacoustic imaging in dentistry: a review on studies over the last decade. Saudi Dent J 2023;35(5):423-36. doi:10.1016/j.sdentj.2023.05.013
30. Hacker L, Joseph J, Lilaj L, Manohar S, Ivory AM, Tao R, et al. Tutorial on phantoms for photoacoustic imaging applications. J Biomed Opt 2024;29(8):080801. doi:10.1117/1.Jbo.29.8.080801
31. Hobson N, Polster SP, Cao Y, Flemming K, Shu Y, Huston J, et al. Phantom validation of quantitative susceptibility and dynamic contrast-enhanced permeability MR sequences across instruments and sites. J Magn Reson Imaging 2020;51(4):1192-9. doi:10.1002/jmri.26927
32. Hacker L, Ivory AM, Joseph J, Gröhl J, Zeqiri B, Rajagopal S, et al. A stable phantom material for optical and acoustic imaging. J Vis Exp 2023(196): e65475. doi:10.3791/65475
33. Jiang D, Zhu L, Tong S, Shen Y, Gao F, Gao F. Photoacoustic imaging plus X: a review. J Biomed Opt 2024;29(Suppl 1): S11513. doi:10.1117/1.Jbo.29.S1.S11513
34. Periyasamy V, Rangaraj M, Pramanik M. Photoacoustic imaging of teeth for dentine imaging and enamel characterization. In: Rechmann P, Fried D, eds. Lasers in Dentistry XXIV. Vol 10473. SPIE; 2018. p. 1-6. doi:10.1117/12.2286733
35. Mozaffarzadeh M, Moore C, Barzegar Golmoghani E, Mantri Y, Hariri A, Jorns A, et al. Motion-compensated noninvasive periodontal health monitoring using handheld and motor-based photoacoustic-ultrasound imaging systems. Biomed Opt Express 2021;12(3):1543-58. doi:10.1364/boe.417345
36. Liu X, Li H, Pang M, Liu J, Song X, He R, et al. Photoacoustic imaging in brain disorders: current progress and clinical applications. View (Beijing) 2024;5(4):20240023. doi:10.1002/VIW.20240023
37. He Y, Qin S, Dyer BA, Zhang H, Zhao L, Chen T, et al. Characterizing mechanical and medical imaging properties of polyvinyl chloride-based tissue-mimicking materials. J Appl Clin Med Phys 2019;20(7):176-83. doi:10.1002/acm2.12661
38. Zhang W, Li J, Yang S. Real-time interleaved photoacoustic and ultrasound imaging for guiding interventional procedures. Appl Acoust 2019;156:1-6. doi:10.1016/j.apacoust.2019.06.028
39. Yang X, Zhu G, Miao Y. Calibration of sound intensity instruments based on the double coupler technology. Appl Acoust 2022;199:109008. doi:10.1016/j.apacoust.2022.109008
40. Alifkalaila A, Mitrayana, Widyaningrum R. Photoacoustic imaging system based on diode laser and condenser microphone for characterization of dental anatomy. Int J Adv Sci Eng Inf Technol 2021;11(6):2363-8. doi:10.18517/ijaseit.11.6.12902
41. Rizwan A, Sridharan B, Park JH, Kim D, Vial JC, Kyhm K, et al. Nanophotonic-enhanced photoacoustic imaging for brain tumor detection. J Nanobiotechnology 2025;23(1):170. doi:10.1186/s12951-025-03204-5
42. Wu Y, Wu D, Wen Y, Yang Y, Zhang J, Chi Z, et al. Photoacoustic imaging in visualization of acupuncture mechanisms. Photonics 2025;12(4):365. doi:10.3390/photonics12040365
43. Liu C, Chen J, Zhang Y, Zhu J, Wang L. Five-wavelength optical-resolution photoacoustic microscopy of blood and lymphatic vessels. Adv Photonics 2021;3(1):016002. doi:10.1117/1.AP.3.1.016002
44. Tian C, Shen K, Dong W, Gao F, Wang K, Li J, et al. Image reconstruction from photoacoustic projections. Photonics Insights 2024;3(3): R06. doi:10.3788/PI.2024.R06
45. Aljohani S. Optical coherence tomography angiography (OCTA) characteristics of acute retinal arterial occlusion: a systematic review. Healthcare (Basel) 2025;13(16):2056. doi:10.3390/healthcare13162056
46. Rašiová M, Schlager O, Heiss C, Brodmann M, Olinic DM, Boc V, et al. Adverse reactions after intravascular iodinated contrast media administration and their management. Vasa 2024;53(3):193-203. doi:10.1024/0301-1526/a001122
47. Jeong SY, Suh CH, Kim SJ, Lemere CA, Lim JS, Lee JH. Amyloid-related imaging abnormalities in the era of anti-amyloid beta monoclonal antibodies for Alzheimer's disease: recent updates on clinical and imaging features and MRI monitoring. Korean J Radiol 2024;25(8):726-41. doi: https://doi.org/10.3348/kjr.2024.0105